Electronic Supplementary Information

Buckle-Driven Delamination of Hydrophobic Micro-, Nano-, and Heterostructured Membranes without a Sacrificial Layer

George K. Larsen and Yiping Zhao

Department of Physics and Astronomy, and Nanoscale Science and Engineering Center, University of Georgia, Athens, Georgia 30602

S1. HFTS monolayer

The vapor-deposition of a fluorinated silane monolayer (HFTS) onto the surface of Si/SiO_2 is a crucial step in the fabrication, as membranes do not delaminate without the application of HFTS. The role of the HFTS in the delamination process is not straightforward, and it may play several roles. The primary role is inducing the hydrophobic effect. Clean gold and Si/SiO_2 surfaces are hydrophilic. Thus, initially, the Au/Si interface is hydrophilic/hydrophilic. The addition of the HFTS monolayer onto the thin or porous Si/SiO_2 layer creates a hydrophilic/hydrophobic interface, and water will intercalate through this heterogeneous interface between the two materials.[1] If enough water intercalates through the interface, perhaps assisted by a porous membrane layer and pinholes, the decohesion area will be large enough to initiate a propagating buckling front, and since the thin Si/SiO_2 layer is now hydrophobic, the delaminated membrane will float on the H_2O surface. Similar effects have been seen using hydrophobic Au and hydrophilic SiO_2 in water-assisted lift-off, although in that process the layers were separated using mechanical action instead of using spontaneous buckling.[2] It is also possible that the HFTS reduces that adhesion between the Au and Si/SiO_2 interface, and it is also possible that the HFTS monolayer induces extrinsic compressive stresses within the membrane layer, which would assist the delamination process.

In order to characterize the HFTS layer, first we used spectroscopic ellipsometry to confirm the thickness of the layer deposited onto a Si/SiO_2 surface, and it was found to be 0.880 $\pm$ 0.002 nm. This is shorter than the calculated length of 1.33 nm, but is consistent with other measurements of HFTS monolayer thicknesses reported in the literature.[3, 4] The difference between the calculated length and the measured length has been attributed to tilting and molecular disorder. We also characterized the functional properties of the monolayer by contact angle measurement. We first measured the contact angle, γ, of a 3 µl drop of de-ionized H_2O on the surface of clean 100 nm Si layers that had been deposited onto Si substrates. The contact angle was found to be $\gamma = 31° \pm 1°$. After the HFTS treatment, the contact angle for the same 100 nm Si films was found to be $\gamma = 95° \pm 8°$. These contact angle results are identical to a pristine Si substrate before and after HFTS treatment. Thus, the HFTS treatment creates a hydrophobic monolayer coating on Si/SiO_2 surfaces.

S2. Morphological parameters of the delaminated membranes

Figure S1a shows an SEM image of a two layer stack of delaminated ultrathin Si gratings. The ultrathin Si gratings were fabricated by depositing 40 nm of Si at three different polar angle orientations (-45°, 0°, 45°) of a CD-R template. This is done to ensure the side walls of the grating grooves are well covered by Si. The morphological parameters of the gratings were determined by analysis of the SEM images. The grating pitch was determined to be 1.55 $\pm$ 0.05 µm, and the groove depth and width were found to be 90 $\pm$ 20 nm and 490 $\pm$ 50 nm, respectively. These results match well with the specifications of CD-Rs. The thickness, h, of the Si layer was found to be $h = 90 \pm 7$ nm.

An additional deposition of 2 µm of Si at a polar angle of 86° will create a Si nanorod layer which rests on top of the grating, as shown in Figure S1b. The nanorods are found to be
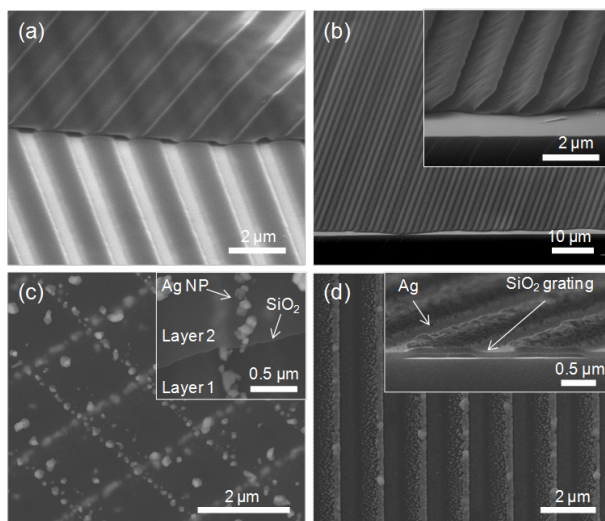
Figure S1. SEM images of a (a) two layer Si grating membrane stack, (b) Si nanorod membrane, (c) two layer Ag nanoparticle coated SiO_2 grating membrane stack, and (d) Ag nanowire coated coated SiO_2 grating membrane, all of which have been transferred onto Si substrates. The insets show higher magnification micrographs of the same film structure.

1.26 ± 0.07 μm in length, and tilt at an angle of $50° \pm 3°$ from the surface normal. The delamination process causes the individual nanorods to clump together in a group on top of the grating. This clumped group is 0.45 ± 0.05 μm in width when measured in the direction perpendicular to the grating grooves.

Figure S1c shows SEM images of Ag nanoparticle coated SiO_2 grating membranes. The Ag nanoparticle (Ag NP) coating was achieved by depositing a thin Ti adhesion layer (~ 15 nm) followed by a thin Ag layer (~ 120 nm), all at an oblique incident angle (86°) onto a SiO_2 layer that was deposited onto a CD-R template using the same process as for the Si grating described above. The Ag aggregates in nanoparticulate form on one side of the grating surface and does not form a continuous film. The average width of the Ag nanoparticles in the direction perpendicular to the grating grooves is found to be 150 ± 50 nm, the average width of the nanoparticles in the direction parallel with the grating grooves is 200 ± 200 nm, and the average nanoparticle separation along the direction of the grating grooves is 70 ± 70 nm. The thickness of the SiO_2 layer was found to be 78 nm within the groove and 96 nm on top of the groove.

By increasing the Ag deposition thickness to 300 nm, a continuous layer of Ag was formed along one side of the CD-R grating, creating an Ag nanowire coated SiO_2 grating membrane (Figure S1b). The continuous Ag coating has an average width in the direction perpendicular to the gratings of 250 ± 40 nm, and the average thickness of the Ag layer is found to be 130 ± 20 nm. The SiO_2 layer is identical to the one describe above for the Ag nanoparticle coated SiO_2 films. In addition to the nanowire coating on one side of the grating grooves, Ag nanoparticles also form on top of the grating grooves.
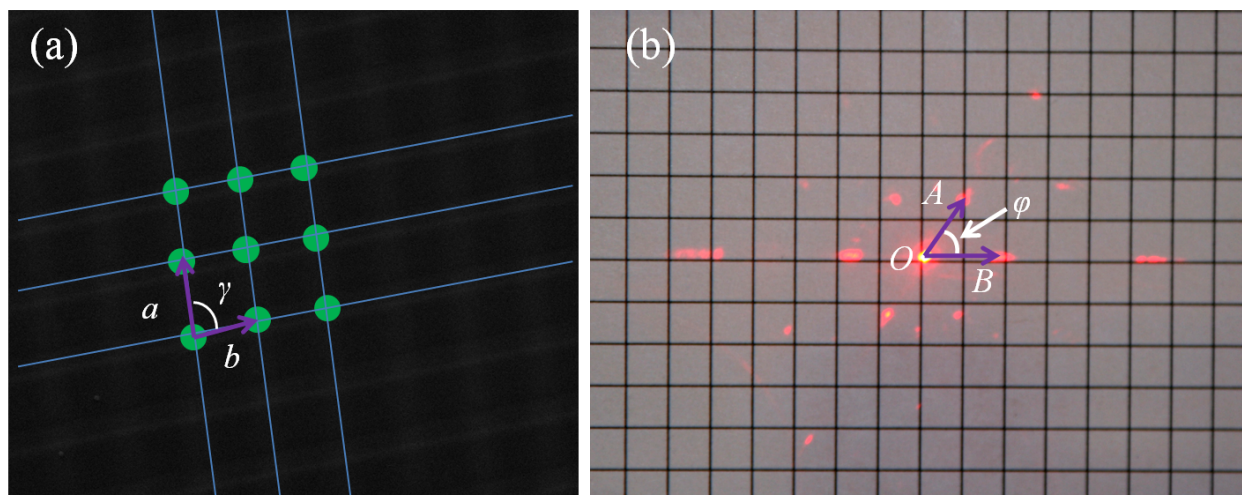
S3. Diffraction images

The diffraction intensity pattern of CD-R without the original Au coating and a one layer ultrathin Si grating (red HeNe laser, $\lambda = 632.8$ nm) are shown in Figure S2. The images of the diffraction spots show that the Si grating diffracts more strongly and has less stray light around m_0 than the original CD-R template. This difference is quantified for different wavelengths by the spectra shown in Figures 2a and 2b of the main article. Note that the grid screen was not in the exact same location for both images, hence the apparent difference in separation between the diffraction orders for the two images.
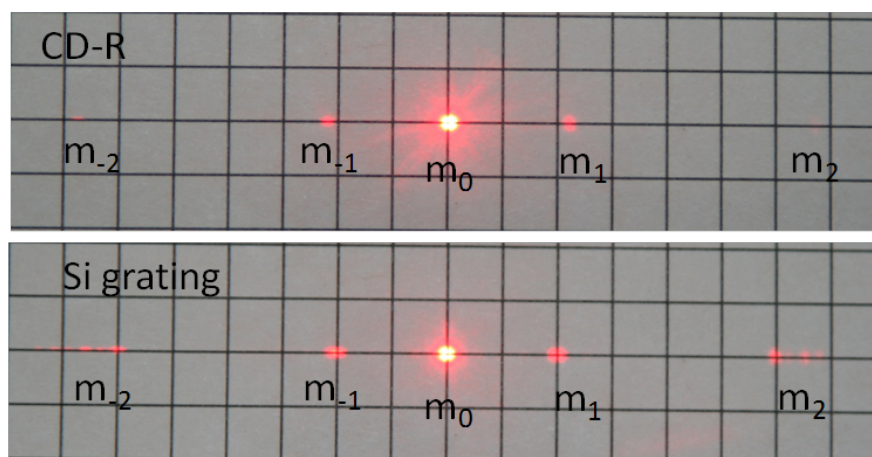
Figure S2. *Diffracted light, $\lambda = 632$ nm, from both the CD-R template and a delaminated ultrathin grating that had been transferred to a glass subsrate.*

The delaminated gratings can also be stacked into multilayers. Figure S3a shows a top-view SEM image of a two layer stack of delaminated ultrathin Si gratings that had been transferred to a clean Si substrate. The overlaying diagram describes the two-dimensional grating parameter notation, where a and b are the lattice spacings in the two different directions and γ is the angle between them. In this case, $a = b = 1.55 \pm 0.05$ µm, therefore the only distinguishing feature between the two directions is that a corresponds with the upper layer, while b corresponds with the lower layer. If γ is defined to be the angle from a to b, in a clockwise manner, then $\gamma = 83° \pm 3°$. Figure S3b shows the laser diffraction pattern of a different two layer stack that had been transferred to a glass substrate. The zeroth order diffraction spot O is in the center, and there are 6 first order diffraction spots that encircle O. The nearest neighbor first order diffraction spots, A and B, form an angle, $\varphi = 60° \pm 2°$. It is important to note that A, B, and φ are related to the reciprocal lattice parameters, a^*, b^*, and γ^* of the two-dimensional grating.

Figure S3. *(a) Top-view SEM image of a two layer stack of delaminated ultrathin Si gratings that had been transferred to a Si substrate, and (b) diffraction pattern from a different two layer stack of ultrathin Si gratings that had transferred to a glass substrate. Note that the diffraction pattern (b) is not generated from sample (a).*

S4. Rigorous coupled wave analysis of the grating structures

The observation that the delaminated gratings can diffract light more efficiently than the original CD-R template is unexpected (Figure 3a and 3b of the manuscript). In order to confirm that such effects can occur on a theoretical basis, we used an open source rigorous coupled wave analysis solver (RCWA, RODIS 1.2.c) to calculate the zero-, first-, and second-order diffraction efficiencies over the wavelength region 300-800 nm using simulated structures that approximate the morphologies of the CD-R and the delaminated grating membranes. The simulated structures of the CD-R grating and delaminated Si ultrathin grating are illustrated in Figures S4a and S4b, respectively. Through the RCWA electromagnetics simulation, we found that, even though the zero-order (transmission) efficiency, η_0, for the simulated CD-R structure was greater than that of the simulated grating membrane structure (Figure S4c), the first- and second-order diffraction
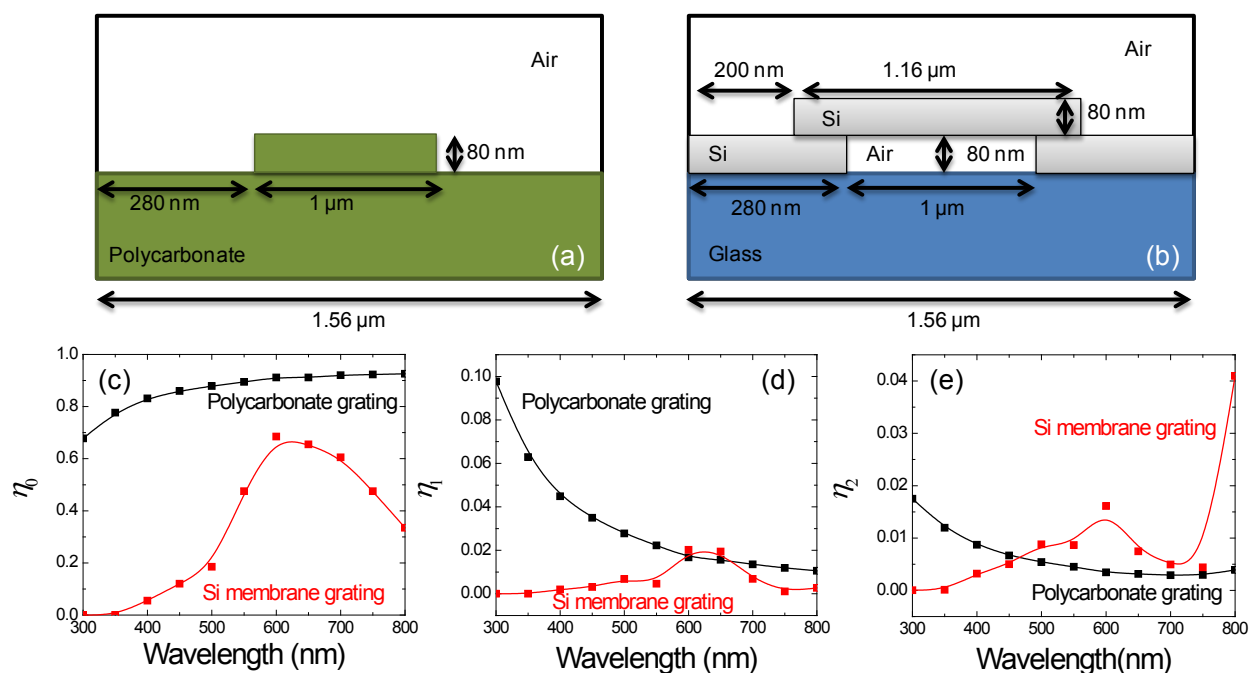
Figure S4 Illustration of the structures used in the RCWA calculation: (a) CD-R grating and (b) delaminated Si grating adhered to a glass substrate. (c) - (d) RCWA results for the different order diffraction efficiencies η_0, η_1, and η_2, respectively. The squares denote the data points, and the solid curve is a B-spline fit of the data.

efficiencies, η_1 and η_2, of the simulated grating membrane can exceed those of the CD-R in the wavelength region $\lambda = 500 - 800$ nm (Figures S4d and S4e, respectively). These results agree qualitatively with our experimental results, confirming that such effects are consistent with electromagnetic theory. The quantitative discrepancy between the simulations and experimental measurements in the ratio of η_1^{Si}/η_1^{CD} (compare Figure 3b in the manuscript and Figure S4d) is attributed to the idealization of the structures for simulation and to using standard optical constants of the materials.[5]

S5. Pattern transfer fidelity for patterned membranes

The impact of the delamination process on morphologies of patterned shapes is an important consideration. The primary effects are illustrated in Figures S5a – S5f. In particular, a Si thin film appears as a flat disk prior to delamination (Figure S5a), but after delamination two competing processes can affect the morphology: buckling and wrinkling due to heterogeneous
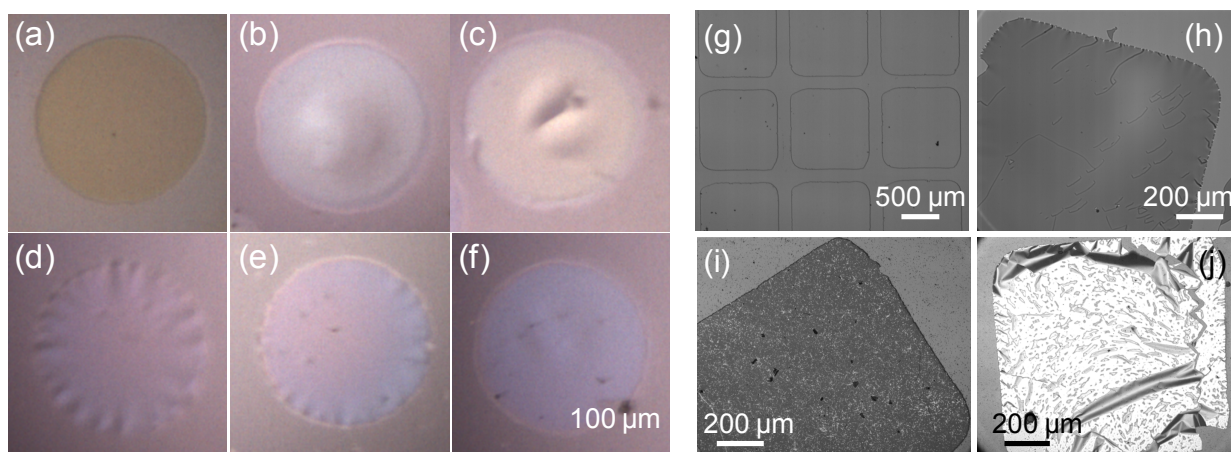
Figure S5 *Optical micrographs of a Si disk membrane (a) attached to the original Ag substrate prior to delamination and (b)-(f) delaminated Si disks floating on the surface of water with different thicknesses h: (b) h ≈ 70 nm; (c) h ≈ 80 nm; (d) h ≈ 90 nm; (e) h ≈ 100 nm; and (f) h ≈ 110 nm. Optical micrographs of (g) Si square membrane attached to the original Ag substrate prior to delamination; (h) Si square membrane delaminated and floating on the surface of water; (i) Si square membrane delaminated and transferred to a clean Si substrate; (j) Si square membrane delaminated and transferred to a clean Ag nanorod array substrate.*

stresses and substrate/membrane interactions. As shown in Figures S5b – S5f, the compressive stress within the Si layer causes the membrane to buckle away from the H_2O/Si interface, but the adhesive energy of the interface causes portions of the buckled/wrinkled regions to drape back toward the H_2O surface. These effects have been exploited in the fabrication of strained-silicon-on-silicon devices and in the fabrication of micro-/nanochannel networks.[6, 7] In Figures S5b – S5f, it appears that the thicker membranes exhibit better pattern transfer fidelity, with the 110 nm membrane appearing as a flat Si disk while floating on the surface of H_2O. However, the relationship between thickness and pattern fidelity is not necessarily straightforward in the hydrophobic Si/SiO_2 membranes. Different thicknesses will exhibit different magnitudes of stress and can vary from tensile to compressive.[8] Furthermore, the silane monolayer can induce extrinsic stresses within the Si/SiO_2 which can create a thickness-dependent stress gradient profile, and, additionally, the monolayer can change the interface energy, where the nature of the interface will depend on the distance between the substrate and the fluorinated silane molecules bonded to Si/SiO_2 surfaces. These thickness dependence effects on buckle/wrinkle formation and interface energy will determine the morphology of the membrane after delamination.

In addition to the membrane properties, capillary forces and the properties of the underlying substrate (e.g., stiffness, surface energy, etc.) can affect the morphology of the membrane. The effect of the interface/substrate on the morphology of delaminated patterned membranes is illustrated in Figures S5g – S5j. Figure S5g shows a 100 nm-thick Si square membrane (~1 mm^2) prior to delamination attached to the original Ag substrate. After delamination, the square exhibits some cracking due to spalling, but also some wrinkles can be observed along the edges (Figure 5h) due to capillary forces and the liquid substrate. After transferring the membrane to solid substrates, the nature of the interface changes which causes a

change in the morphology of the membrane. For example, Figure 5i shows the morphology of a delaminated 100 nm Si square transferred to a Si substrate, which is very stiff and hydrophilic. Ignoring the cracks and missing pieces formed by spallation during delamination, the morphology of the delaminated membrane is identical to the original morphology; it is a flat Si thin film without wrinkles. On the other hand, Figure 5j shows the morphology of a delaminated 100 nm Si square membrane transferred to the surface of an Ag nanorod array film. The Ag nanorod array is more hydrophobic and less stiff than the Si substrate, and the 100 nm Si square membrane exhibits wrinkling and buckling throughout.

S6. Experimental details of membrane characterization

Imaging was performed by optical microscopy and scanning electron microscopy (FEI Inspect field emission SEM). Transmission diffraction of the Si grating and CD-R grating (with the original Au coating removed) was characterized using a 100 watt QTH lamp (Newport Corp., Apex) and a monochromator (Newport Corp., Cornerstone) for illumination, and a moveable amplified Si detector (Newport Corp.) attached to a lock-in amplifier (Newport Corp., Merlin) for signal detection. UV-visible absorbance spectroscopy was characterized using a double beam spectrophotometer (Jasco V-570) in transmission mode. For the SERS measurements, 5 μl of 100 μM MPh solution in ethanol (MPh, Sigma-Aldrich, 97%) was dropped onto the films and allowed to dry. The SERS spectra of MPh were acquired by a HRC-10HT Raman analyzer (Enwave Optronics Inc.), with a laser beam of 785 nm excitation wavelength, 30 mW output power, 100 μm laser spot diameter, and a collection time of 10 s. The HFTS monolayer thickness measurement was performed using a variable angle spectroscopic ellipsometer (J.A. Woollam Co., Inc., M-2000) at incident angles 65°, 70°, and 75°. Prior to HFTS treatment, the Si substrate was measured and modeled as a Si substrate with a native oxide layer (thickness,

1.39 nm) within the software (CompleteEASE v.4.85). After HFTS treatment, the substrate was measured and modeled again using the same parameters for the Si substrate, but with an additional Cauchy layer. The Cauchy layer thickness was the only fitting parameter, as the optical constants of the Cauchy layer were fixed at $A = 1.349$, and $B = C = k = 0$. The fitting resulted in a thickness of 0.880 ± 0.002 nm with MSE = 0.731. The contact angle measurements of the Si films and Si substrate were performed, before and after HFTS treatment, by the sessile drop method (Data Physics OCA 20) using a 3 μl drop of de-ionized H_2O.

References:

1.   G. F. Schneider, V. E. Calado, H. Zandbergen, L. M. Vandersypen and C. Dekker, *Nano Lett.*, 2010, **10**, 1912-1916.
2.   M. Donolato, C. Tollan, J. M. Porro, A. Berger and P. Vavassori, *Adv. Mater.*, 2013, **25**, 623-629.
3.   R. E. Geer, D. A. Stenger, M. S. Chen, J. M. Calvert, R. Shashidhar, Y. H. Jeong and P. S. Pershan, *Langmuir*, 1994, **10**, 1171-1176.
4.   A. Hozumi, K. Ushiyama, H. Sugimura and O. Takai, *Langmuir*, 1999, **15**, 7600-7604.
5.   E. D. Palik, *Handbook of Optical Constants of Solids: Index*, Access Online via Elsevier, 1998.
6.   G. M. Cohen, P. M. Mooney, V. K. Paruchuri and H. J. Hovel, *Appl. Phys. Lett.*, 2005, **86**, 251902.
7.   Y. Mei, D. J. Thurmer, F. Cavallo, S. Kiravittaya and O. G. Schmidt, *Adv. Mater.*, 2007, **19**, 2124-2128.
8.   L. B. Freund and S. Suresh, *Thin film materials: stress, defect formation and surface evolution*, Cambridge University Press, 2004.